MARCH 12 2026

Multipath correlation at mid-frequency in a convergence zone

F. Hunter Akins ; William S. Hodgkiss

J. Acoust. Soc. Am. 159, 2189–2198 (2026)
https://doi.org/10.1121/10.0042988

JASA ARTICLE

GQ1

Multipath correlation at mid-frequency in a convergence zone

F. Hunter Akins[a)] and William S. Hodgkiss
Scripps Institution of Oceanography, University of California San Diego, La Jolla, California 92093, USA

ABSTRACT:
Convergence zone (CZ) propagation is characterized by a small number of eigenrays, each with one deep ocean turning point and no more than two upper ocean turning points. Because of this geometry, these rays undergo a small amount of random internal wave scattering relative to the CZ range of ~ 60 km. It is hypothesized that CZ multipath will therefore be correlated over limited observation intervals. The theory of wave propagation in random media is applied to CZ propagation through a Garrett–Munk internal wave field to predict the correlation between CZ eigenrays at mid-frequency over a finite observation interval. The theoretical results predict correlated multipath over intervals between 100 and 200 s. This prediction is then compared to data collected during an experiment in the Philippine Sea. The complex amplitudes of multipath arrivals in the CZ from 5.5 kHz sinusoidal transmissions are estimated using beamforming with a vertical line array and seen to be significantly correlated over approximately 27 s. https://doi.org/10.1121/10.0042988

(Received 29 August 2025; revised 16 February 2026; accepted 18 February 2026; published online 12 March 2026)

[Editor: John A. Colosi] Pages: 2189–2198

I. INTRODUCTION

In many array processing applications, the sample correlation matrix is estimated from data and subsequently used to mitigate the deleterious effects of correlated noise and interference (Baggeroer *et al.*, 1993; Cox *et al.*, 1987). This work presents theoretical calculations and experimental results to explore multipath signal correlations in convergence zone (CZ) acoustic propagation at mid-frequency, defined here as the frequency range from 1 to 10 kHz.

In underwater acoustic propagation, interaction with the sea surface, rough seafloor, and volume inhomegeneities causes scattering and adds random perturbations to the acoustic pressure field (Colosi, 2016; Eckart, 1953; Jones *et al.*, 2014). The precise effect of scattering depends on the acoustic wavelength as well as the temporal and spatial correlation of medium inhomegeneities or boundary roughness. CZ propagation is relatively long range propagation (~ 60 km) with no boundary interactions (Urick, 1965). As a result, in the absence of source and receiver motion, scattering along ray paths within the ocean volume provides the only means to decorrelate multipath arrivals from a single source. This work applies the theory of wave propagation in random media (WPRM) (Tatarskii, 1961; Chernov, 1960) to predict the decorrelating effect from fluctuations due to internal wave driven ocean inhomegeneities in mid-frequency CZ propagation (Flatté *et al.*, 1979; Munk and Zachariasen, 1976). Previous work theoretically analyzed correlations between ray paths over internal wave ensembles toward the goal of making acoustic measurements of the internal wave field (Flatté and Stoughton, 1986). This work focuses on the correlation of ray arrival complex amplitudes over limited observation periods. The calculations made here for 5.5 kHz CZ propagation predict that multipath arrivals, while uncorrelated over ensembles of internal wave realizations, will remain correlated over intervals between 100 and 200 s.

The theoretical predictions are then compared to experimental data collected in the Philippine Sea in 2019. During the experiment, tonal transmissions were made from a stationary source lowered beneath the Research Vessel (R/V) Sally Ride to a depth of 150 m and were received on a vertical line array (VLA) located in the CZ at a range of $\sim$59 km and a depth of $\sim$143 m. The complex amplitudes of distinct multipath arrivals from 5.5 kHz receptions are estimated with plane wave beamforming over a 5.5 min observation period. The arrivals are observed to be significantly correlated over approximately 27 s.

The paper is organized as follows. Section II introduces notation and the conjugate product of arrival complex amplitudes that is used in the subsequent analysis. Section III applies results from WPRM to mid-frequency multipath propagation in a CZ, and provides a theoretical prediction for the correlation time of mid-frequency multipath arrivals scattered by random internal waves. Section IV analyzes experimental data and compares the observations to the theoretical predictions of Sec. III. Conclusions are provided in Sec. V.

II. DATA MODEL AND ESTIMATION OF SAMPLE CORRELATION MATRIX

The snapshot $\mathbf{d}_k$ is the vector of complex discrete Fourier transform outputs at M elements of a VLA from a time window centered at t_k in a frequency bin of interest. Assume the VLA has uniformly spaced elements and

[a)]Email: fakins@ucsd.edu

https://doi.org/10.1121/10.0042988

measures N_s plane wave multipath arrivals from a single sinusoidal source at frequency ω. For a propagation speed c in the vicinity of the array and an array element spacing Δz, the steering vector for an arrival at an incident angle θ is

$$\mathbf{a}(\theta) = \left[1 \;\; e^{-j\omega/c\Delta z \sin\theta} \;\; \ldots \;\; e^{-j\omega/c(M-1)\Delta z \sin\theta}\right]^T. \tag{1}$$

In this work, the sign convention of the Fourier transform used to form snapshots, together with the indexing of array elements from deepest to shallowest, is such that steering vectors with positive angles correspond to arrivals coming from below. Let $\mathbf{A}$ be the $M \times N_s$ matrix

$$\mathbf{A} = [\mathbf{a}(\theta_0) \;\; \mathbf{a}(\theta_1) \;\; \ldots \;\; \mathbf{a}(\theta_{N_s-1})], \tag{2}$$

whose columns are the steering vectors of the N_s arrivals with angles $\theta_0, \theta_1, \ldots, \theta_{N_s-1}$. Let $\mathbf{s}_k$ be the vector of complex amplitudes of the N_s arrivals at time t_k, and let $\mathbf{n}_k$ be an additive noise component. The kth snapshot can then be written as

$$\mathbf{d}_k = \mathbf{A}\mathbf{s}_k + \mathbf{n}_k. \tag{3}$$

Both the noise component $\mathbf{n}_k$ and the amplitudes in $\mathbf{s}_k$ are modeled as zero-mean stationary Gaussian random processes. This statistical model will later be shown to apply to mid-frequency CZ propagation through a random Gaussian internal wave field.

The spatial correlation matrix $\mathbf{R} \equiv \mathrm{E}(\mathbf{d}\mathbf{d}^H)$, where $\mathrm{E}(\cdot)$ denotes expectation, plays a central role in many array processing algorithms (Johnson and Dudgeon, 1993).[1] For the data model in Eq. (3),

$$\mathbf{R} = \mathbf{A}\mathbf{S}\mathbf{A}^H + \mathbf{R}_n, \tag{4}$$

where $(\mathbf{S})_{ij} = \mathrm{E}(s_i s_j^*)$ is the inter-signal correlation matrix, and $\mathbf{R}_n$ is the noise correlation matrix. In practice, the spatial correlation matrix is unknown *a priori* and is estimated from the data using the sample correlation matrix

$$\hat{\mathbf{R}} = \frac{1}{N}\sum_{k=0}^{N-1} \mathbf{d}_k \mathbf{d}_k^H. \tag{5}$$

Assuming that the sample cross correlation between the noise and plane wave signal amplitudes is approximately 0, we can write the data sample correlation matrix

$$\hat{\mathbf{R}} \approx \mathbf{A}\hat{\mathbf{S}}\mathbf{A}^H + \hat{\mathbf{R}}_n \tag{6}$$

in terms of the matrix $\mathbf{A}$, the signal sample correlation matrix $\hat{\mathbf{S}}$, and the noise sample correlation matrix $\hat{\mathbf{R}}_n$. Array processing algorithms exploit the structure of the sample correlation matrix and should take account of correlated multipath, which manifests as significant off diagonal components in $\hat{\mathbf{S}}$.

Each element of the matrix $\hat{\mathbf{S}}$ is the sample mean of the conjugate product $x_{ij}[t_k] = s_i[t_k]s_j^*[t_k]$ of the ith and jth arrival amplitudes in the kth snapshot. The variance of $(\hat{\mathbf{S}})_{ij}$ is determined both by the number of snapshots N and the autocorrelation function (ACF) of x_{ij} (Box and Jenkins, 1976). The correlation time of x_{ij} therefore provides a characteristic scale that informs the properties of the sample correlation matrix. Roughly speaking, for intervals much shorter than the correlation time of x_{ij}, arrivals will appear correlated regardless of their true (infinite time average) correlation. This work studies the correlation time of x_{ij} specifically for mid-frequency signal arrivals in a CZ.

III. MID-FREQUENCY MULTIPATH CORRELATION IN THE CONVERGENCE ZONE THROUGH AN INTERNAL WAVE FIELD

A ray trace for a 150 m deep source through a typical deep water profile is shown in Fig. 1. Figure 1 shows purely refracted rays (no boundary interactions) that bend toward the seafloor because of the downward refracting thermocline at the source depth before turning at great depth and converging at the surface at a range of approximately 58–61 km to form the CZ. Because of the absence of boundary interactions and the focusing effect of refraction, the CZ is a region of relatively high intensity. In the geometric approximation to the wave equation, valid at mid-frequency in the CZ, the pressure field is described by a sum over rays that connect the source and receiver; such rays are referred to as eigenrays. Each eigenray has a complex amplitude,

$$s_i(t) = A_i(t)e^{-j\omega\tau_i(t)}, \tag{7}$$

and a local orientation θ_i with respect to the horizontal. A complex source amplitude, which is common to all rays

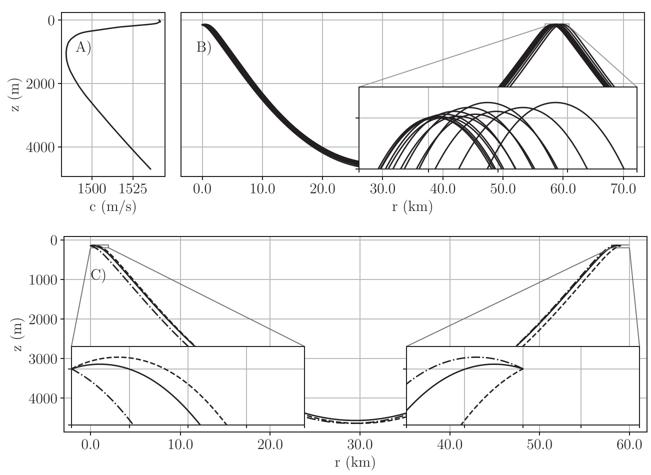

FIG. 1. (A) Background sound speed profile and (B) ray trace for a source at 150 m depth. Only non-boundary interacting rays are shown. The inset in (B) shows the CZ and spans the depth from 120 to 200 m depth and the range from 57 to 61 km. (C) CZ eigenrays with no boundary interactions for a source depth of 150 m, receiver depth of 150 m, and receiver range of 59 km. Both insets span the depths from 130 to 200 m and have a horizontal extent of 2 km. All rays have at least one turning point near the surface, with the shallow launch angle ray turning near both the source and the receiver. The two steepest launch angle rays (dashed and dash-dotted curves) are reflections of one another about the midpoint of propagation. The shallow launch angle ray (solid curve) is symmetric about the midpoint.

produced by a single source, is ignored in Eq. (7). The term $A_i(t)$, which represents the propagation effects of geometric spreading and focusing of the wavefront, is therefore real-valued. The phase $-\omega\tau_i(t)$ is determined by the source frequency ω and the eigenray travel time $\tau_i(t)$ through the medium. Over an aperture for which the sound speed is approximately constant, the curvature of the eigenray wavefronts is negligible, and each eigenray corresponds to a plane wave arrival. In this work, the time dependence of the amplitude and phase are assumed to be because of the time-variability of the medium. Depending on the source frequency, the ray paths, and the medium properties, the time variability of the eigenrays may be correlated or uncorrelated.

Theoretical results from the theory of WPRM (Colosi, 2015; Flatté *et al.*, 1979; Tatarskii, 1961) are now applied to predict the correlation between mid-frequency CZ eigenrays. The ocean sound speed profile $c(r,z,t)$ is modeled as

$$c(r,z,t) = c_0(z) + \Delta c(r,z,t), \tag{8}$$

where $c_0(z)$ is a known, static background profile, and $\Delta c(r,z,t) \ll c_0(z)$ is a random perturbation. The sound speed perturbation is assumed to be the result of adiabatic internal wave displacement of water parcels,

$$\Delta c(r,z,t) = \zeta(r,z,t)\frac{\mathrm{d}c_p(z)}{\mathrm{d}z}, \tag{9}$$

where $\zeta(r,z,t)$ is the internal wave displacement field, and $\mathrm{d}c_p(z)/\mathrm{d}z$ is the potential sound speed depth gradient (Munk and Zachariasen, 1976). The displacement ζ is statistically modeled by a zero-mean Gaussian random process that is stationary in both the horizontal and in time. Its ACF R_ζ is determined by the Garrett–Munk spectrum (Garrett and Munk, 1972) and the background buoyancy frequency profile $N_0(z)$. From Eq. (9), the sound speed perturbation is also a zero-mean Gaussian process with both horizontal spatial and temporal stationarity and with ACF,

$$\begin{aligned} &R_{\Delta c}(r_2-r_1,z_1,z_2,T) \\ &\quad = \frac{\mathrm{d}c_p(z_1)}{\mathrm{d}z}R_\zeta(r_2-r_1,z_1,z_2,T)\frac{\mathrm{d}c_p(z_2)}{\mathrm{d}z}. \end{aligned} \tag{10}$$

Here, r_2-r_1 denotes the separation of two points in range, z_1 and z_2 denote their respective depths, and T denotes their offset in time.

Wave propagation through a random medium can be classified as unsaturated, partially saturated, or fully saturated, depending on the frequency of sound, the geometry of propagation, and the statistics of the random medium (Colosi, 2015; Flatté *et al.*, 1979). Mid-frequency CZ propagation through a random Garrett–Munk internal wave field was previously reported to be partially saturated (Akins *et al.*, 2024) using the regime boundary definitions of (Colosi, 2016). In this regime, the amplitude of each eigenray varies much more slowly than its phase. Therefore, it is a good approximation to consider only the variation in phase when considering the correlation time of mid-frequency CZ multipaths. That is,

$$s_i(t) \approx A_i e^{-j\omega\tau_i(t)} \tag{11}$$

for constant A_i. The preceding section showed that the sample correlation between multipath arrivals depends on the length of the observation interval relative to the correlation time of the conjugate product $x_{ij}(t) = s_i(t)s_j^*(t)$ of eigenray complex amplitudes. Therefore, x_{ij} is the primary quantity of interest in this work, and its ACF provides insight into correlation between multipath arrivals over a finite observation interval. This is in contrast to the correlation between arrivals over all internal wave realizations, which is quantified by $\mathrm{E}(x_{ij})$.

In the geometric acoustics, partially saturated regime, under the constant amplitude approximation in Eq. (11), the ACF of x_{ij} is

$$R_{x_{ij}}(t_1,t_2) = \sigma_{ij}^2\mathrm{E}\left(e^{-j\omega\left([\tau_i(t_1)-\tau_i(t_2)]-[\tau_j(t_1)-\tau_j(t_2)]\right)}\right), \tag{12}$$

where $\sigma_{ij}^2 = \mathrm{E}(A_i^2A_j^2)$. For jointly stationary Gaussian τ_i and τ_j, this is equal to

$$\begin{aligned} R_{x_{ij}}(T) = \sigma_{ij}^2 \times \exp\bigg(&-\frac{1}{2}\omega^2\mathrm{E}\Big(\big([\tau_i(t)-\tau_i(t+T)] \\ &-[\tau_j(t)-\tau_j(t+T)]\big)^2\Big)\bigg), \end{aligned} \tag{13}$$

which is real-valued and depends only on the lag time $T = t_2 - t_1$. For mid-frequency CZ propagation, it is therefore sufficient to consider the joint statistics of eigenray travel times to characterize the multipath correlation observed in a finite observation interval.

A. Travel time statistics

The eigenray travel time τ_i is an integral of the slowness $c^{-1}(r,z,t)$ along the ray path Γ_i,

$$\tau_i(t) = \int_{\Gamma_i}(c_0(z(s)) + \Delta c(r(s),z(s),t))^{-1}\mathrm{d}s. \tag{14}$$

The explicit dependence of the depth and range on the path length variable s will be henceforth suppressed for notational convenience. Using the small perturbation approximation $\Delta c \ll c_0$, this can be written to good approximation as

$$\tau_i(t) = \bar{\tau}_i - \int_{\Gamma_i}\frac{\Delta c(r,z,t)}{c_0(z)}\mathrm{d}s. \tag{15}$$

Because of the Gaussian properties of the perturbation Δc, τ_i is a Gaussian random process with mean $\bar{\tau}_i$ and autocovariance function,

$$C_{\tau_i\tau_i}(T) = \int_{\Gamma_i}\int_{\Gamma_i} \frac{R_{\Delta c}(r-r',z,z',T)}{c_0^2(z)c_0^2(z')}\,\mathrm{d}s\,\mathrm{d}s'. \quad (16)$$

Similarly, the cross-covariance between the travel times of two eigenrays is

$$C_{\tau_i\tau_j}(T) = \int_{\Gamma_i}\int_{\Gamma_j} \frac{R_{\Delta c}(r'-r,z,z',T)}{c_0^2(z)c_0^2(z')}\,\mathrm{d}s\,\mathrm{d}s'. \quad (17)$$

Because of the time stationarity of the sound speed perturbation, the travel times of a pair of eigenrays are jointly stationary.

From Eq. (13), the correlation between multipath arrivals over a finite interval depends on the correlation time of the travel time difference,

$$\Delta\tau_{ij}(t) = (\tau_i(t)-\overline{\tau}_i) - (\tau_j(t)-\overline{\tau}_j). \quad (18)$$

This process is zero mean and has autocovariance function,

$$\begin{aligned} C_{\Delta\tau_{ij}\Delta\tau_{ij}}(T) &= \mathrm{E}(\Delta\tau_{ij}(t)\Delta\tau_{ij}(t+T)) \\ &= C_{\tau_i\tau_i}(T) + C_{\tau_j\tau_j}(T) - 2C_{\tau_i\tau_j}(T). \end{aligned} \quad (19)$$

After some manipulations, the ACF of the conjugate product of eigenray complex amplitudes in Eq. (13) can be expressed in terms of $C_{\Delta\tau_{ij}\Delta\tau_{ij}}$ as

$$R_{x_{ij}}(T) = \sigma_{ij}^2 \exp\Big(-\omega^2\big(C_{\Delta\tau_{ij}\Delta\tau_{ij}}(0) - C_{\Delta\tau_{ij}\Delta\tau_{ij}}(T)\big)\Big). \quad (20)$$

In particular, the normalized cross correlation $R_{x_{ij}}(T)/\sigma_{ij}^2$ will be used to define a correlation time. In this work, the correlation time T_c is defined to be the time at which the normalized ACF of x_{ij} drops to one-half,

$$R_{x_{ij}}(T_c)/\sigma_{ij}^2 = \frac{1}{2}. \quad (21)$$

As will be shown below, the ACF $R_{x_{ij}}(T)$ [Eq. (20)] is approximately Gaussian for lags T that are small compared to the time scales of the internal wave displacements. This is derived here using the same method that Flatté *et al.* (1979) use to derive that the ACF of a single ray arrival complex amplitude is approximately Gaussian for short time lags. Consider the power spectral density (PSD) of sound speed perturbations,

$$\mathcal{S}_{\Delta c}(r-r',z,z',f) = \int_{-\infty}^{\infty} R_{\Delta c}(r-r',z,z',T)e^{-j2\pi fT}dT. \quad (22)$$

Note here that the frequency f of the sound speed perturbations in cycles per unit time is distinct from ω, which denotes the acoustic frequency in rad / s. The integrals in Eqs. (16) and (17) can be written in terms of the PSD as

$$C_{\tau_i\tau_j}(T) = 2\int_0^{\infty}\int_{\Gamma_i}\int_{\Gamma_j} \frac{\mathcal{S}_{\Delta c}(r-r',z,z',f)}{c_0^2(z)c_0^2(z')}\cos fT\,\mathrm{d}f\,\mathrm{d}s\mathrm{d}s', \quad (23)$$

where the conjugate symmetry of the PSD $\mathcal{S}$ is used to perform the inverse Fourier transform over the positive frequency axis. The negative of the argument of the exponential of $R_{x_{ij}}$ [Eq. (20)], expanded out and grouped into three terms, is

$$\begin{aligned} &\omega^2(C_{\tau_i\tau_i}(0) - C_{\tau_i\tau_i}(T)) + \omega^2(C_{\tau_j\tau_j}(0) - C_{\tau_j\tau_j}(T)) \\ &\quad - 2\omega^2(C_{\tau_i\tau_j}(0) - C_{\tau_i\tau_j}(T)). \end{aligned} \quad (24)$$

The first two terms are (ignoring a factor of 2) the phase structure functions of the ith and jth eigenrays (Flatté *et al.*, 1979) and tend to decrease the ACF of x_{ij} as the individual arrivals become decorrelated. The third term accounts for the correlation between the travel times of the two eigenrays, increasing the ACF of x_{ij} when changes in the individual eigenray travel times are correlated. As an aside, the common case of rays with turning points that are well-separated compared to the spatial correlation length of sound speed perturbations, the third term is negligible, and the correlation time of x_{ij} can be calculated simply in terms of the phase structure functions of the individual eigenrays. Using Eq. (23), these three terms can be computed as

$$\begin{aligned} C_{\tau_i\tau_j}(0) - C_{\tau_i\tau_j}(T) = 2\int_0^{\infty}\int_{\Gamma_i}\int_{\Gamma_j} &\frac{\mathcal{S}_{\Delta c}(r'-r,z,z',f)}{c_0^2(z)c_0^2(z')} \\ &\times(1-\cos fT)\,\mathrm{d}f\,\mathrm{d}s\mathrm{d}s'. \end{aligned} \quad (25)$$

Using the Taylor expansion of $\cos fT$ for small fT, this is approximately

$$\begin{aligned} &C_{\tau_i\tau_j}(0) - C_{\tau_i\tau_j}(T) \\ &\quad\approx 2T^2\int_0^{f_c}\int_{\Gamma_i}\int_{\Gamma_j} \frac{f^2\mathcal{S}_{\Delta c}(r'-r,z,z',f)}{c_0^2(z)c_0^2(z')}\,\mathrm{d}f\,\mathrm{d}s\mathrm{d}s', \end{aligned} \quad (26)$$

which is equal to the quadratic term T^2 multiplied by a constant determined by the triple integral. The Garrett–Munk spectrum is dominated by energy in the near-inertial range and drops off as f^{-2} away from the inertial frequency. It also has zero energy above the cutoff frequency f_c, which is the maximum buoyancy frequency in the water and therefore has replaced ∞ in the upper limit of the integral above. For T less than $1/f_c$, on the order of 5 min in the thermocline, the Taylor series converges for all frequencies in the integral and is an excellent approximation over the dominant low-frequency part of the spectrum. With this approximation, the ACF takes on the form

$$R_{x_{ij}}(T) \approx \sigma_{ij}^2 e^{-T^2/\kappa_{ij}^2}, \quad (27)$$

where the correlation scale κ_{ij} is a constant independent of time and is related to the defined correlation time by $T_c = \sqrt{\log 2}\cdot\kappa_{ij}$. As will be seen in the numerical results of the subsequent section, for the lag times T on the order of a few minutes considered in this work, the Gaussian ACF is an excellent approximation to $R_{x_{ij}}$.

https://doi.org/10.1121/10.0042988

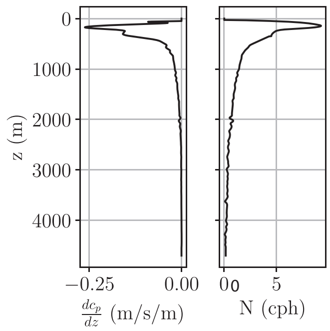

FIG. 2. Background potential sound speed gradient (left) and buoyancy profile $N_0(z)$ (right) in cycles per hour (cph) obtained from CTD measurements from the experiment and used for the numerical calculations of Sec. III.

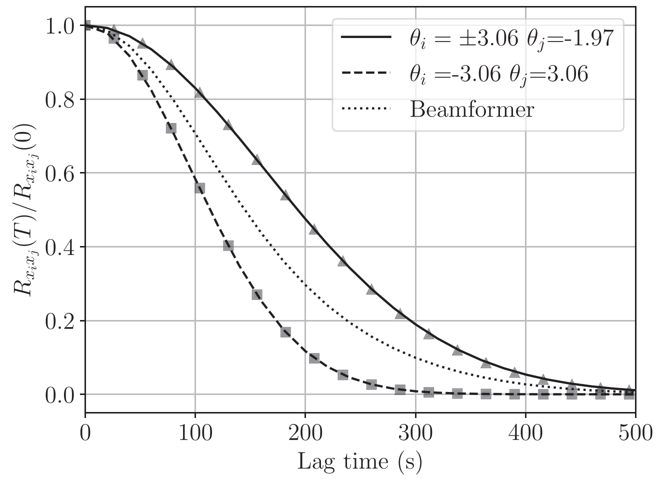

FIG. 3. The WPRM numerical calculations of the normalized ACFs $R_{x_{ij}}(T)/\sigma_{ij}^2$ of the conjugate product $x_{ij}(t) = s_i(t)s_j^*(t)$ for pairs of the three eigenrays at 59 km range are shown as solid and dashed lines. The triangle and square symbols indicate the corresponding Gaussian approximations to the normalized ACFs. The symbols essentially coincide with the numerically calculated normalized ACF (solid and dashed lines, respectively). The rays are identified by their launch angle. $\theta > 0$ indicates a ray oriented toward the seafloor. The dotted line added here gives the normalized autocorrelation of the conjugate of up- and down-looking beamformer outputs. The up-looking output contains an equal sum of two eigenrays with launch angles of 3.06° and −1.97° (corresponding to arrivals coming from the surface in the CZ). The downward-looking output consists purely of the eigenray with launch angle −3.06°.

In summary, the ACF $R_{x_{ij}}$ of the conjugate product $x_{ij}(t) = s_i(t)s_j(t)^*$ of two eigenray complex amplitudes is used to characterize the sample multipath correlation from a finite observation interval. For geometric acoustics and partial saturation, the normalized ACF is determined by the joint statistics of eigenray travel times. For the random medium model considered here, it is sufficient to compute the covariances of eigenray travel times [Eqs. (16) and (17)], which are used to compute $R_{x_{ij}}$ in Eq. (20). The correlation time T_c for a pair of eigenray arrivals is then defined in terms of $R_{x_{ij}}$ in Eq. (21). Finally, the ACF $R_{x_{ij}}$ has an approximately Gaussian form for short time lags, a result that is evident in the numerical results of the subsequent section.

B. Numerical results

The formulas of the preceding section are now applied to 5.5 kHz CZ propagation for a source at a depth of 150 m and a receiver at a depth of 150 m and a range of 59 km.[2] At this range, there are three purely refracted eigenrays, shown in Fig. 1, with launch angles of approximately +3°, −2°, and −3° (positive angle oriented toward the seafloor). The corresponding angles of arrival are −3°, −2°, and +3°. The rays with launch angles of ±3° have a single shallow turning point, occurring near the source for the −3° ray and near the receiver for the +3° ray. The ray with a launch angle of −2° has two near-surface turning points: one near the source and the other near the receiver. All CZ rays have a single deep turning point. Note that the ±3° rays form a reciprocal pair, in that exchanging the source and receiver converts one to the other.

To produce predictions for comparison with the experimental data, the sound speed correlation function $R_{\Delta c}$ was computed using a potential sound speed gradient $\mathrm{d}c_p/\mathrm{d}z$ and buoyancy frequency $N_0(z)$ estimated from conductivity-temperature-depth (CTD) measurements made during the experiment and shown in Fig. 2. In particular, the potential sound speed profile $c_p(z)$ was computed from *in situ* measurements of temperature and salinity using the Thermodynamic Equation of Seawater 2010 (TEOS-10; McDougall and Barker, 2011), and the potential sound speed gradient $\mathrm{d}c_p/\mathrm{d}z$ was computed from a spline fit to $c_p(z)$. Using $N_0(z)$, the internal wave modes were computed for horizontal wavenumbers on a mesh from 0.0035 to 0.5 cycles per km for modes up to $J = 20$ (Evans, 2000). The modes were then used to compute the displacement correlation function R_ζ sampled on a 10 m depth grid, a 2 km grid for the horizontal lag, and a 20 s grid for time lag using the following Garrett–Munk spectrum parameters: energy density $E_0 = 4000$ J m^{-2} and mode number roll-off $j_* = 3$ (Winters and D'Asaro, 1997). Using $\mathrm{d}c_p/\mathrm{d}z$, the sound speed correlation $R_{\Delta c}$ was then computed using Eq. (10). The functions $C_{\tau_i\tau_i}$ and $C_{\tau_i\tau_j}$ were then evaluated numerically for each eigenray / pair of eigenrays for each sampled lag time $T = 0$, $T = 20$ s, …, $T = 500$ s. Finally, the ACF $R_{x_{ij}}$ of the conjugate product of eigenray complex amplitudes Eq. (20) was computed for the same time lags.

The normalized ACF $R_{x_{ij}}(T)/\sigma_{ij}^2$ for the various eigenray pairs is shown in Fig. 3 along with a Gaussian function with the same correlation time. The ACFs are seen to have nearly Gaussian forms and correlation times between 100 and 200 s. Because of the reciprocal relationship of the ±3° rays, the ACF of the conjugate product of +3° and −2° ray complex amplitudes is identical to that of the −3° and −2° ray complex amplitudes. The decorrelation time between +3° and −3° rays is shorter than that between the ±3° and −2° rays. This is reasonable considering that the turning points of +3° and −3° occur nearly 60 km apart, which is much longer than the spatial correlation length of the sound speed perturbations. In comparison, the −2° ray shares one turning point with each of the other two rays, and so there is only one turning point where uncorrelated perturbations cause the phases of the eigenrays in the pair to drift apart.

In the experiment, eigenray amplitudes are not directly observed. Instead, multipath amplitudes are estimated with a VLA using beamforming. The measured amplitudes therefore correspond to a weighted sum of eigenray amplitudes, with significant contributions from rays whose arrival angles fall within the array angular resolution. The ACF of the conjugate product of beamformer outputs can be computed in terms of the eigenray auto-/cross-covariances [Eqs. (16) and (17)] and the relative contribution of each eigenray to the beamformer outputs. This function is shown in Fig. 3 for the specific case of an upward looking beam with equal contributions from the -2° and $+3^\circ$ launch angle eigenrays and a downward looking beam with the single eigenray with launch angle -3°.

IV. EXPERIMENTAL MEASUREMENTS AND COMPARISON TO THEORY

This section presents experimental measurements of mid-frequency CZ multipath made in the Philippine Sea in 2019 for comparison to the theoretical predictions of Sec. III. During the experiment, transmissions were made from an ITC-1007 source (International Transducer Corporation, Santa Barbara, CA, USA) suspended on a cable 150 m below the R/V Sally Ride, which used dynamic positioning to maintain a constant position at approximately 14.85°N, 141.5°E. The source transmitted a repeating sequence of 30 s of tonals at frequencies from 1.5 to 7.5 kHz followed by 30 s without transmission. The transmissions were recorded for a period of 15 min with a sample rate of 25 kHz on an array located in the CZ at a range of $\sim$59 km and a depth of approximately 143 m. The array was tethered to a buoy that freely drifted during the experiment. Analysis of the Global Positioning System on the ship and the drifting buoy during the transmissions showed a relative displacement between the source and receiver of approximately 10 m over the 5.5 min of transmissions selected for analysis (described below). The ship and buoy positions are shown in Fig. 4 over a bathymetric map of the experiment area [General Bathymetric Chart of the Oceans (GEBCO), 2025]. The water depth is approximately 4800 m along the transmission path.

The vertical array consists of 64 elements spaced at 1/8 m ($\lambda/2$ at 6 kHz). Of the various transmitted tonals, the 5.5 kHz tonal was selected for analysis as it had the smallest beam width of the tonals with no spatial aliasing. Snapshots for the 5.5 kHz tonal transmission were first formed with a short time Fourier transform using a segment length of 25 000 samples (1 s) with a Hann window and a 50% overlap, corresponding to a sample interval of $\Delta t = 0.5$ s. Plane wave beamforming using a Kaiser–Bessel window with $\alpha = 2/\pi$, defined as in Harris (1978), is applied to the snapshots. From the 15 min transmission, 5.5 min were identified during which the VLA could clearly separate distinct multipath arrivals. This 5.5 min period started at April 20, 2019 [Julian Day (JD) 110] at 03:42 UTC.

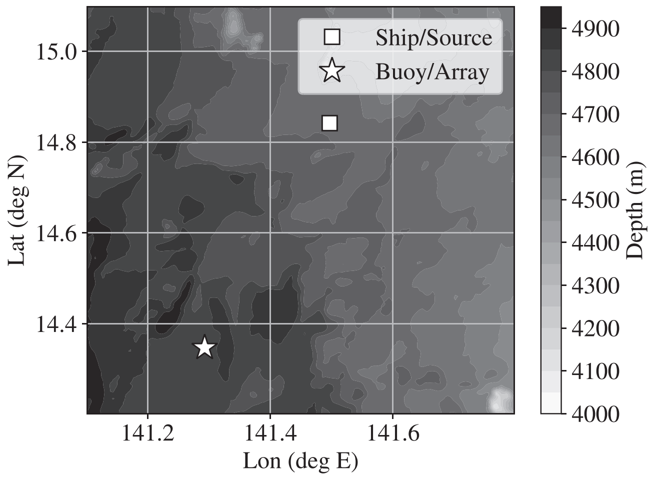

FIG. 4. Positions of the ship (source) and buoy (receiver array) during the analyzed transmissions over a map of the bathymetry in the region (GEBCO 2025). During the 5.5 min of analyzed data, the buoy drifted by $\sim$10 m, which is imperceptible on the scale of this figure. The ship maintained a nearly constant position. The water depth is approximately 4800 m along the transmission path. Lat, Latitude; Lon, Longitude.

The beamformer output during this 5.5 min period for 5.5 kHz snapshots is shown in Fig. 5. From each 30 s transmitting segment, the upward- and downward-looking angles with the highest beamformer output power were identified (indicated with a white star in Fig. 5). Then, the conjugate product of the beamformer outputs corresponding to these angles was formed,

$$\chi[t_k] = B_{up}[t_k]B^*_{down}[t_k]. \tag{28}$$

The magnitude and phase of this quantity is shown in Fig. 5. Note that the phase $\angle\chi$ is the phase difference between the upward- and downward-looking beams.

The output of the beamformer in a given look direction contains contributions from arrivals within the mainlobe as well as the sidelobes. Therefore, χ is not a direct sample of the conjugate product $x_{ij}(t)$ of eigenray complex amplitudes that was analyzed theoretically in Sec. III. Instead, it is a weighted sum of the conjugate product of all pairs of eigenray complex amplitudes that contribute to the two beamformer outputs B_{up} and B_{down}. For the VLA, frequency, and spatial window used here, the broadside beam pattern has a peak-to-sidelobe ratio of approximately 20 dB and a half-power beam width of approximately 2°. Analysis with high-resolution spectral estimation (Tufts and Kumaresan, 1982), not detailed here, indicates that the broader, upward-looking beam seen in Fig. 5 contains two closely spaced arrivals near 0° and -2°, with the steeper arrival near -2° having twice the magnitude of the arrival near broadside. Meanwhile, the downward-looking beam at 4° contains a single arrival. The upward-looking beam B_{up} identified for analysis contains contributions from the two closely spaced arrivals, but given the difference in their magnitude and the mainlobe beampattern, it is dominated by the arrival near -2°. Note also that the predicted correlation time for an equal contribution of two eigenrays in one beam and a

https://doi.org/10.1121/10.0042988

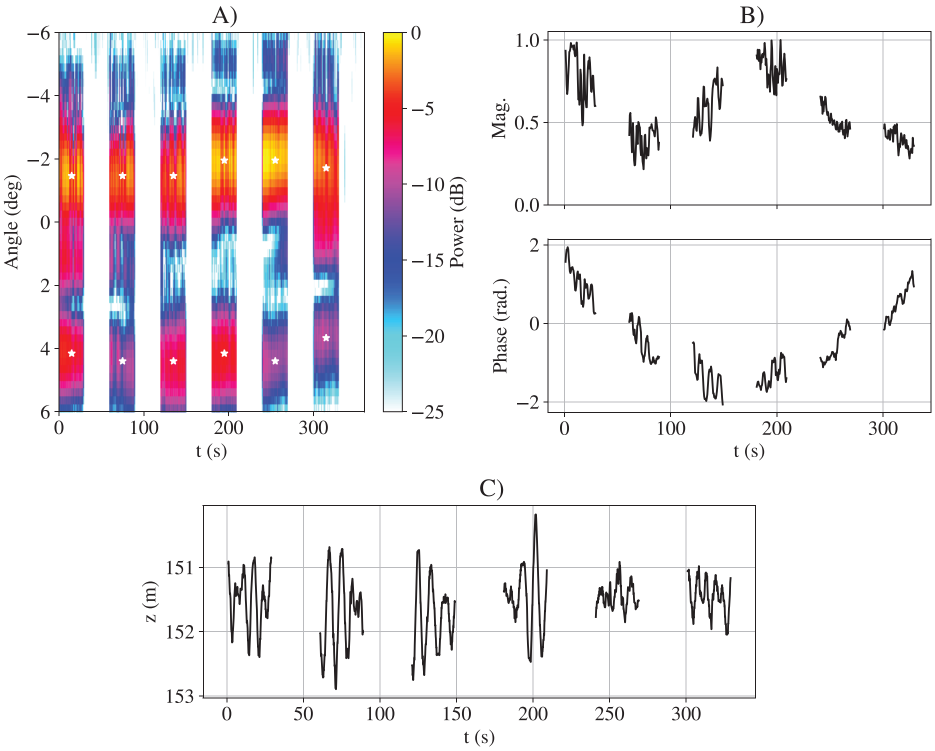

FIG. 5. (A) Beamformer output power during stationary source transmissions. Time is measured in seconds since April 20 (JD110) 2019 03:42 UTC. The angle convention is such that negative angles correspond to rays arriving from above. The white star indicates the upward- and downward-looking beams selected for the correlation analysis. (B) Relative magnitude (top) and phase (bottom) of the conjugate product of the upward- and downward-looking beamformer outputs. The phase of this process is the phase difference between the two beams. The 8 s period oscillations in phase are correlated with depth changes in the source motion because of surface waves. The longer time scale fluctuation is consistent with the scale of predicted phase changes from internal wave driven ocean variability. (C) Measured source depth during the transmission period.

single eigenray in another beam is also shown in Fig. 3 and is seen to be comparable to that of two isolated eigenrays.

Examining the phase of χ in Fig. 5, it has oscillations of $\sim$1 rad on the relatively short time scale of $\sim$10 s as well as a longer time scale variation in the range of nearly 5 rad. The short time scale oscillations are highly correlated with measurements of the source depth made by a pressure (depth) sensor during transmissions, also shown in Fig. 5. The phase response of a ray to a change in source depth depends on the ray launch angle. To get a rough sense of the scale of this effect, consider two-plane waves with launch angles of $+2^\circ$ and -2° at 5.5 kHz. A 1 m change in source depth changes the phase difference between these two waves by 1.6 rad, which is comparable to the $\sim$1 rad variations seen in Fig. 5. The short time oscillations also appear correlated with variations in the magnitude of χ and the beamformer output, for example from 120 to 150 s.

The longer time scale variation in the phase difference is thought to be because of internal wave driven variability in the ocean during the transmission period. The scale and time evolution of this observed phase difference variability is comparable to that reported by DeFilippis *et al.* (2025, their Fig. 4b). There, the phase difference between a direct path and a refracted path with a single upper turning point at a range of $\sim$2 km varied smoothly over a 30 min period and showed similar changes of $\sim$3 rad over periods of 5 min at 4 kHz. Despite the much greater range of the CZ propagation analyzed here, the sensitivity to internal wave scattering is not much different from the close range example analyzed there because of the small number of CZ turning points in the upper ocean.

The WPRM calculations presented in Sec. III and summarized in Fig. 3 predict that the conjugate product of CZ eigenray arrivals has an approximately Gaussian ACF and a correlation time between 100 and 200 s. As discussed previously, the conjugate product of beamformer outputs χ is considered to be dominated by the conjugate product x_{ij} of two eigenray arrivals. It is therefore modeled here as a direct measurement of x_{ij} (for unspecified i and j), plus additive zero-mean white Gaussian noise ξ of variance σ_n^2,

$$\chi[t_k] = x_{ij}[t_k] + \xi[t_k]. \tag{29}$$

The observations of χ can be compared to the theoretical correlation function of x_{ij} using the sample ACF estimator

$$\hat{R}_\chi[l] = \frac{1}{N-l}\sum_{k=0}^{N-l-1} \chi[t_k]\chi^*[t_{k+l}]. \tag{30}$$

Using the Gaussian approximation to $R_{x_{ij}}$ Eq. (27), χ has the approximate ACF,

$$R_\chi(T) = \begin{cases} \sigma_{ij}^2 e^{-T^2/\kappa_{ij}^2} & \text{for } T > 0 \\ \sigma_{ij}^2 + \sigma_n^2 & \text{for } T = 0. \end{cases} \tag{31}$$

The measurements $\{\chi[t_0], \chi[t_1], \ldots, \chi[t_{N-1}]\}$, stored in a vector $\boldsymbol{\chi}$, then obey a multivariate Gaussian distribution as

$$p(\boldsymbol{\chi}; \kappa, \sigma_{ij}, \sigma_n) = \frac{e^{-1/2(\boldsymbol{\chi}^\dagger \mathbf{R}^{-1}\boldsymbol{\chi})}}{\sqrt{2\pi \det(\mathbf{R})}}, \tag{32}$$

where the elements of the covariance matrix $(\mathbf{R})_{ij} = R_\chi(t_i - t_j)$ are the ACF of χ [Eq. (31)] evaluated at the time lag $t_i - t_j$ between the ith and jth samples of χ.

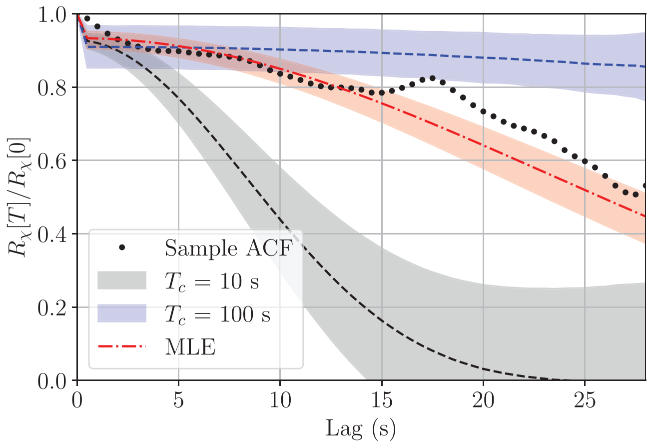

FIG. 6. Analysis of the ACF $R_\chi[l]$ of the conjugate product $\chi[t_k] = B_{up}[t_k]B^*_{down}[t_k]$ of upward- and downward-looking beams using both the normalized sample ACF estimator $\hat{R}_\chi[l]/\hat{R}_\chi[0]$ and parameter estimation using the theoretical ACF of Eq. (31). Black dots show the real part of the normalized sample ACF estimator. The imaginary part, not shown, is everywhere <0.1. The black and blue dashed lines and shaded regions are theoretical results that demonstrate the mean and one standard deviation regions of the real part of the sample ACF estimator applied to time samples of a random process, equivalent to those of the data, with correlation times of 10 s and 100 s, respectively. These illustrate the relatively high variance of the sample ACF estimator at lags beyond a few seconds. The red dash-dotted line and shaded red region depict the MLE of the normalized ACF with one standard deviation uncertainty. The estimated parameters correspond to a SNR of 11.5 dB and a correlation time $T_c = 27$ s.

Figure 6 shows the estimation of R_χ using the sample ACF estimator [Eq. (30)] for the observations of χ. Recall that from the experiment, there are 5.5 min of samples of χ at a 2 Hz sample rate, with 30 s gaps every other 30 s (see Fig. 5). The mean and standard deviation of the sample ACF estimator applied to an analogous set of samples $\chi[t]$ can be analyzed by Monte Carlo integration. Specifically, for a given correlation scale κ_{ij}, signal standard deviation σ_{ij}, and noise standard deviation σ_n, random realizations of $\boldsymbol{\chi}$ can be generated using the probability distribution in Eq. (32). Then, the sample ACF estimator $\hat{R}_\chi$ is applied to the random realizations of $\boldsymbol{\chi}$ to obtain an ensemble of estimates. Figure 6 shows the mean and one standard-deviation region from 1000 realizations of the ACF estimator $\hat{R}_\chi(T)$ for correlation times $T_c = 10$ s and $T_c = 100$ s. For both correlation times, the signal-to-noise ratio (SNR) was chosen to match the estimated SNR of 11.5 dB reported in the subsequent paragraph. In general, the sample ACF estimates have fairly high variance: even for the 10 s correlation time, the 5.5 min of data (with 30 s gaps) results in a 68% confidence interval between ∼0.3 and 0.6 at the 10 s lag. These theoretical calculations demonstrate that the correlation time T_c will generally be poorly estimated by computing the lag at which the normalized sample ACF drops to 0.5. Nonetheless, the fact that the sample ACF estimator values from the measurements of χ fall between the two theoretical regions indicates that the samples of χ are likely to come from a distribution with $10 < T_c < 100$ s.

As an alternative to the direct sample ACF estimator [Eq. (30)], the parameters σ_{ij}, σ_n, and κ_{ij} of the assumed probability density function (PDF) of $\boldsymbol{\chi}$ [Eq. (32)] can also be estimated from the data by maximum likelihood estimation. The Nelder–Mead simplex algorithm was used to maximize the PDF over the parameters. The corresponding maximum likelihood estimates (MLEs) of the distribution parameters were $\hat{\kappa}_{ij} = 32.6$, $\hat{\sigma}_{ij} = 0.59$, and $\hat{\sigma}_n = 0.16$, corresponding to an estimated correlation time of $\hat{T}_c = 27$ s and an estimated SNR of 11.5 dB. The theoretical normalized ACF [Eq. (31)] corresponding to these maximum likelihood estimates is also shown in Fig. 6. Monte Carlo integration was used to estimate the mean and variance of the maximum likelihood estimator applied to analogous samples from the experiment (5.5 min with 30 s gaps) drawn from the distribution of $\boldsymbol{\chi}$ with the parameters set to the MLEs. In particular, 1000 realizations of $\boldsymbol{\chi}$ were drawn using Eq. (32) with $\kappa_{ij} = \hat{\kappa}_{ij}$, $\sigma_{ij} = \hat{\sigma}_{ij}$ and $\sigma_n = \hat{\sigma}_n$ and used for maximum likelihood estimation. The sample mean of the estimated parameter values agreed with the true values within 0.1%, indicating that the estimator was correctly implemented and is unbiased. The one standard deviation uncertainties of the parameters are as follows: 3.09 s for κ_{ij} (corresponding to 2.6 s for $\hat{T}_c$), 0.09 for σ_{ij}, and 0.004 for σ_n. The estimator realizations were also used to compute the one standard deviation uncertainty of the estimated normalized ACF, shown as the red shaded region in Fig. 6.

The comparison between the sample ACF from the measurements of χ to the theoretical performance of the sample ACF provides good confidence that the correlation time is between 10 and 100 s. Under the assumption, motivated by the WPRM results, that the samples of χ are Gaussian distributed with a Gaussian ACF (plus a white noise diagonal loading), the maximum likelihood estimation of the distribution parameters correspond to an estimated correlation time T_c of x_{ij} equal to 27 ± 2.6 s (one standard deviation uncertainty). This estimate, though shorter than the 100 s to 200 s WPRM calculation, is thought to be in rough agreement with the theoretical predictions.

No single, clear explanation was found for the discrepancy between the observed and predicted correlation time. Rather, it is thought that several factors may contribute. First, the true internal wave spectral parameters were not measured during the experiment, and any mismatch with the canonical values used herein introduces error into the prediction. The predicted correlation time was not found to change significantly in response to changes to the wavenumber grid parameters nor the modal cutoff number j_* or maximum mode number J. It can be derived from Eq. (26) that the correlation time $T_c \propto E_0^{-1/2}$. Therefore, a doubling of the internal wave field energy density reduces the predicted correlation time by a factor of $\sqrt{2}$ (e.g., from 100 to ∼70 s). In fact, such a doubling was reported by Colosi *et al.* (2019) in their analysis of data collected during the Philippine Sea (PhilSea10) experiment. Second, many experiments have reported an excess in internal wave energy over the Garrett–Munk spectrum in the upper ocean at frequencies near the buoyancy frequency (Roth *et al.*, 1981). The longer time scale phase variation ascribed to internal wave activity in Fig. 5(B) is suggestive of a fluctuation

https://doi.org/10.1121/10.0042988

with a period of approximately 5 min, close to the internal wave cutoff frequency (the maximum buoyancy frequency minus the inertial frequency). Furthermore, the turning point depths of the CZ eigenrays studied here occur near the depth of the buoyancy frequency maximum, and a displacement of just half of a meter in the vicinity of a turning point is enough to change the phase of an eigenray by 1 rad. It is therefore conceivable that the shorter observed correlation time is because of sound speed variability driven by internal waves near the cutoff frequency, whose strength are underestimated by the Garrett–Munk spectrum. Finally, the predictions do not consider variations in the arrival amplitudes nor the decorrelating effects of source depth variations. The predicted correlation time is not highly sensitive to reasonable variations of these factors, and so the observed discrepancy may be a result of their combined effects.

V. CONCLUSION

Multipath arrivals in the CZ travel along purely refracted rays with no more than two upper ocean turning points and therefore undergo limited scattering by internal wave driven inhomogeneities. The conjugate product $x_{ij} = s_i s_j^*$ of two arrivals s_i and s_j was analyzed to investigate the correlation between CZ multipath present over finite observation intervals. In particular, the correlation time T_c of the autocorrelation function $R_{x_{ij}}$ of x_{ij}, defined by the lag time at which $R_{x_{ij}}$ drops to half its value at zero lag, is a characteristic temporal scale over which arrivals will be correlated. WPRM theory was used to numerically compute $R_{x_{ij}}$ for 5.5 kHz CZ arrivals and predicted a correlation time between 100 and 200 s. For these arrivals, $R_{x_{ij}}$ was also seen to have an approximately Gaussian form. The theoretical predictions were then compared to 5.5 kHz tonal transmissions recorded on a VLA in the CZ during an experiment in the Philippine Sea. Complex amplitudes of two identified arrivals were estimated with plane wave beamforming over a 5.5 min period. The correlation time T_c of $R_{x_{ij}}$ was found to lie between 10 and 100 s. By assuming that $R_{x_{ij}}$ has a Gaussian form and that the beamformer outputs are dominated by individual arrival amplitudes plus white Gaussian noise, the probability distribution of the measurements is characterized by the parameters of $R_{x_{ij}}$ and the white noise level. These assumptions are supported by the theoretical results and analysis of the data. The parameters of this distribution were estimated by maximum likelihood estimation and correspond to a correlation time of $\sim$27 s for the multipath arrival complex amplitudes estimated by beamforming. The analysis and experimental data indicate that the strength of internal wave perturbations and their temporal correlation are such that mid-frequency multipath arrivals in the CZ will be correlated on time scales on the order of tens of seconds, although further experiments should verify the robustness of this observation.

ACKNOWLEDGMENTS

This research was inspired in part by the late Dr. William Kuperman. This research was supported by the Office of Naval Research (ONR) under Grant No. N00014-23-1–2557. Dave Ensberg helped with data access.

AUTHOR DECLARATIONS

Conflict of Interest

The authors have no conflicts to disclose.

DATA AVAILABILITY

The acoustic data that support the findings of this study are available on request from W.S.H., subject to sponsor restrictions.

[1]Note the correlation definition here, which follows that of Papoulis (1984), differs from the definition of correlation as the normalized autocovariance often used in statistics.

[2]Note that from Eq. (17) the correlation time T_c is proportional to the inverse of the acoustic frequency. Therefore, the correlation times for other frequencies for which the geometric, partially saturated propagation regime applies can be obtained by rescaling the result reported here.

Akins, F. H., Hodgkiss, W. S., and Kuperman, W. A. (**2024**). "Phase stability of convergence zone propagation at mid-frequency," J. Acoust. Soc. Am. **156**(4), 2409–2421.

Baggeroer, A., Kuperman, W., and Mikhalevsky, P. (**1993**). "An overview of matched field methods in ocean acoustics," IEEE J. Ocean. Eng. **18**(4), 401–424.

Box, G. E. P., and Jenkins, G. M. (**1976**). *Time Series Analysis: Forecasting and Control*, rev. ed. (Holden-Day, San Francisco).

Chernov, L. A. (**1960**). *Wave Propagation in a Random Medium* (Dover, New York).

Colosi, J. A. (**2015**). "A reformulation of the Λ-Φ diagram for the prediction of ocean acoustic fluctuation regimes," J. Acoust. Soc. Am. **137**(5), 2485–2494.

Colosi, J. A. (**2016**). *Sound Propagation through the Stochastic Ocean* (Cambridge University Press, New York).

Colosi, J. A., Cornuelle, B. D., Dzieciuch, M. A., Worcester, P. F., and Chandrayadula, T. K. (**2019**). "Observations of phase and intensity fluctuations for low-frequency, long-range transmissions in the Philippine Sea and comparisons to path-integral theory," J. Acoust. Soc. Am. **146**(1), 567–585.

Cox, H., Zeskind, R., and Owen, M. (**1987**). "Robust adaptive beamforming," IEEE Trans. Acoust. Speech. Signal Process. **35**(10), 1365–1376.

DeFilippis, J. P., Cornuelle, B. D., Lucas, A. J., Hodgkiss, W. S., and Kuperman, W. A. (**2025**). "Measuring phase difference to sense small-scale ocean sound-speed structure," JASA Express Lett. **5**(2), 020801.

Eckart, C. (**1953**). "The scattering of sound from the sea surface," J. Acoust. Soc. Am. **25**(3), 566–570.

Evans, R. (**2000**). "Memorandum: Calculation of internal wave eigenfrequencies and modes; displacement; sound speed realizations," https://oalib-acoustics.org/website_resources/Other/wave/Wave.pdf (Last viewed August 15, 2025).

Flatté, S. M., Dashen, R. F., Munk, W. H. W. H., Watson, K. M., and Zachariasen, F. (**1979**). *Cambridge Monographs on Mechanics and Applied Mathematics Sound Transmission through a Fluctuating Ocean* (Cambridge University Press, Cambridge, UK).

Flatté, S. M., and Stoughton, R. B. (**1986**). "Theory of acoustic measurement of internal wave strength as a function of depth, horizontal position, and time," J. Geophys. Res. Oceans **91**(C6), 7709–7720.

Garrett, C., and Munk, W. (**1972**). "Space-time scales of internal waves," Geophys. Fluid Dyn. **3**(3), 225–264.

GEBCO. (**2025**). "The GEBCO 2025 Grid," https://www.gebco.net/data-products-gridded-bathymetry-data/gebco2025-grid (Last viewed August 15, 2025).

Harris, F. (**1978**). "On the use of windows for harmonic analysis with the discrete Fourier transform," Proc. IEEE **66**(1), 51–83.

Johnson, D. H., and Dudgeon, D. E. (**1993**). *Array Signal Processing: Concepts and Techniques* (Prentice Hall, Englewood Cliffs, NJ).

https://doi.org/10.1121/10.0042988

Jones, B. A., Colosi, J. A., and Stanton, T. K. (**2014**). "Echo statistics of individual and aggregations of scatterers in the water column of a random, oceanic waveguide," J. Acoust. Soc. Am. **136**(1), 90–108.

McDougall, T. J., and Barker, P. M. (**2011**). *Getting Started with TEOS-10 and the Gibbs Seawater (GSW) Oceanographic Toolbox* (SCOR/IAPSO WG127, Newark, DE), p. 28.

Munk, W. H., and Zachariasen, F. (**1976**). "Sound propagation through a fluctuating stratified ocean: Theory and observation," J. Acoust. Soc. Am. **59**(4), 818–838.

Papoulis, A. (**1984**). *Probability, Random Variables, and Stochastic Processes*, 2nd ed., McGraw-Hill Series in Electrical Engineering (McGraw-Hill, New York).

Roth, M. W., Briscoe, M. G., and McComas, C. H. (**1981**). "Internal waves in the upper ocean," J. Phys. Oceanogr. **11**(9), 1234–1247.

Tatarskii, V. I. (**1961**). *Wave Propagation in a Turbulent Medium* (McGraw-Hill, New York).

Tufts, D., and Kumaresan, R. (**1982**). "Estimation of frequencies of multiple sinusoids: Making linear prediction perform like maximum likelihood," Proc. IEEE **70**(9), 975–989.

Urick, R. J. (**1965**). "Caustics and convergence zones in deep-water sound transmission," J. Acoust. Soc. Am. **38**(2), 348–358.

Winters, K. B., and D'Asaro, E. A. (**1997**). "Direct simulation of internal wave energy transfer," J. Phys. Oceanogr. **27**(9), 1937–1945.